

Article

Low-Temperature Manufacture of Cubic-Phase $\text{Li}_7\text{La}_3\text{Zr}_2\text{O}_{12}$ Electrolyte for All-Solid-State Batteries by Bed Powder

Taehong Park [†], Sunho Lee [†]  and Dong-Min Kim ^{*}

Department of Materials Science and Engineering, Hongik University, Sejong 30016, Republic of Korea; pth3983@g.hongik.ac.kr (T.P.); sunho0710@g.hongik.ac.kr (S.L.)

^{*} Correspondence: dmkim@hongik.ac.kr

[†] These authors contributed equally to this work.

Abstract: As the demand for battery technology with enhanced safety and high energy density increases, solid-state batteries are currently attracting attention as a solution to problems such as fire and explosion risks associated with lithium-ion batteries. In this study, experiments were conducted to synthesize and optimize $\text{Li}_7\text{La}_3\text{Zr}_2\text{O}_{12}$ (LLZO), a solid electrolyte that is a key component of lithium-ion batteries with stability and high energy density. Experimental results showed that sintering at a low temperature of 800 °C for 8 h was the optimal synthesis and sintering time. Additionally, the excess lithium-containing bed powder enabled the production of pure cubic-phase LLZO. Through a sintering process that creates a lithium atmosphere on the bottom surface and facilitates lithium replenishment, an additional tunnel was introduced between the specimen and the alumina powder, allowing the bottom surface of the specimen to be exposed to the lithium atmosphere. By manufacturing a uniform cubic electrolyte, the path to manufacturing all-solid-state batteries was opened. These findings provide a new approach to forming cubic-phase LLZO with much higher ionic conductivity than the tetragonal phase at low sintering temperatures.

Keywords: solid-state battery; electrolyte; LLZO; ionic conductivity



Citation: Park, T.; Lee, S.; Kim, D.-M. Low-Temperature Manufacture of Cubic-Phase $\text{Li}_7\text{La}_3\text{Zr}_2\text{O}_{12}$ Electrolyte for All-Solid-State Batteries by Bed Powder. *Crystals* **2024**, *14*, 271. <https://doi.org/10.3390/cryst14030271>

Academic Editors: Suresh Kannan Balasingam and Manu Gautam

Received: 5 February 2024

Revised: 8 March 2024

Accepted: 8 March 2024

Published: 11 March 2024



Copyright: © 2024 by the authors. Licensee MDPI, Basel, Switzerland. This article is an open access article distributed under the terms and conditions of the Creative Commons Attribution (CC BY) license (<https://creativecommons.org/licenses/by/4.0/>).

1. Introduction

Secondary batteries are designed to utilize the energy generated by chemical reactions as electricity and reuse it through charging and discharging. There are various types of secondary batteries, including lead acid batteries, nickel cadmium batteries, nickel hydride batteries, sodium sulfur batteries, and lithium-ion batteries. Among them, lithium-ion batteries are characterized by being lighter, having a higher operating voltage, and having a higher energy density than other secondary batteries. These properties have made it particularly popular in small electronic devices and portable equipment. Additionally, its importance as a battery for automotive applications has increased significantly [1,2]. However, most currently used lithium-ion batteries using organic electrolytes cause serious safety problems such as low chemical stability, evaporation of the liquid electrolyte, and flammability due to vaporization, resulting in potential fire and explosion risks [3]. Since the thermal stability of the electrolyte plays an important role in the durability of the battery, the development of a safer electrolyte is essential [4]. All-solid-state batteries are expected to use a non-flammable or fire-resistant solid electrolyte instead of a flammable organic liquid electrolyte, eliminating the risk of fire and explosion caused by simultaneous internal short circuit and oxygen gas release from the anode. In addition, electrolyte leakage problems from external shocks, such as direct contact accidents between vehicles, can be excluded, thereby improving safety [5–7]. In addition to fire safety, the unstable electrochemical stability, which was a limitation of existing lithium-ion batteries, can be solved with all-solid-state batteries [8]. All-solid-state batteries are expected to be able to further improve energy density by utilizing high-capacity, high-voltage electrode materials

such as lithium metal, which were difficult to apply to existing lithium-ion batteries [8–11]. Unlike liquid electrolytes that require additional space, such as battery packaging exterior materials, solid electrolytes do not require sealing to prevent liquid electrolyte leakage and have a stackable anode structure, enabling a reduction in subsidiary materials and battery volume. Despite these advantages, the commercialization of all-solid-state batteries has been delayed due to the fact that solid electrolytes have lower ionic conductivity than liquid electrolytes [10]. However, the Li⁺ transfer value of the solid electrolyte is higher than that of the liquid electrolyte with a lithium-ion transfer value of 0.5 or less, enabling faster charging and achieving a higher energy density [12]. Much research has been conducted to improve the low ionic conductivity characteristics of solid electrolytes, and among inorganic solid electrolytes, Li₇La₃Zr₂O₁₂ (LLZO), an oxide-based solid electrolyte with a garnet structure, has a high ionic conductivity of $\sim 10^{-3}$ S/cm. It is attracting attention due to its high stability with lithium metal at room temperature [13–15]. LLZO in the garnet structure has cubic (space group $Ia\bar{3}d$) and tetragonal (space group $I4_1/acd$) phases [16,17]. In the cubic phase, lithium ions can move in three directions, whereas in the tetragonal phase, there are lithium-ion conduction channels only in the a and b directions, making the ionic conductivity of the cubic phase about 100 times higher. To prepare LLZO with higher ionic conductivity, cubic phases must be formed. However, it is important to note that the tetragonal phase is thermodynamically more stable at room temperature [16–18]. The properties of LLZO are greatly influenced by the synthesis process. Currently, there are several challenges in fabricating LLZO with desired properties [19]. Due to the low sinterability of cubic-phase LLZO, temperatures above 1100 °C and durations exceeding 10 h are typically required [19]. Additionally, despite various studies attempting to stabilize the cubic phase by creating Li vacancies through doping, sintering of doped LLZO typically requires high temperatures of 1100–1200 °C for 5–15 h [19–21]. High-temperature sintering is one of the most suitable methods to produce garnet with dense microstructure and high mechanical strength, making it suitable for use during battery cycles [22,23], and it can suppress crystal dislocation diffusion of lithium. However, high-temperature processing requires time and effort. As the garnet structure decomposes and lithium volatilizes, a large amount of raw material powder is required, resulting in a decrease in ionic conductivity of 10^{-6} S/cm [24,25]. Additionally, high-temperature sintering may lead to the evaporation of lithium, resulting in stoichiometric deviations, the formation of pores and impurities, and even phase decomposition, which may hinder the formation of cubic phases. Short sintering times deteriorate the quality of LLZO, resulting in higher porosity and lower ionic conductivity. As a result, porous, low-density, low-conductivity ceramics are easily formed. Additionally, studies have shown that the phase transformation from tetragonal to cubic occurs at approximately 650 °C [26,27]. To stabilize the cubic garnet structure of LLZO at low temperatures, approximately 0.4 to 0.5 mol of lithium vacancies are required per molecule, regardless of the pore creation method [28]. In addition, referring to other research results showing that mixing of tetragonal and cubic phases occurs when sufficient Li vacancies are not created, it can be concluded that the tetragonal phase is more likely to appear as the lithium content increases [28]. Kokal et al. successfully fabricated LLZO samples at a low sintering temperature of 900 °C using the Sol–gel Pechini method [29], and Hui Xie et al. successfully fabricated LLZO samples at a low sintering temperature of 750 °C using the solution method [30]. However, Kokal et al. formed a tetragonal phase and exhibited a low ionic conductivity of 3.12×10^{-7} S/cm, whereas Hui Xie et al. formed a cubic phase and exhibited a low ionic conductivity of 2.85×10^{-6} S/cm. It showed conductivity [29,30]. With this in mind, producing LLZO at low temperatures and precisely controlling its chemical and microstructural properties remain difficult, making industrial scale-up of LLZO difficult. Except for some computational work [31,32], there is a lack of significant experimental insight into the relationships between processing, microstructure, transport properties, and the performance of ceramic solid electrolytes. Therefore, efforts are needed to find a method to prepare cubic LLZO at low temperature using the most widely used solid-phase reaction due to its simplicity and scalability [19]. In this study, we

use a systematic experimental approach to compare the microstructural properties obtained by applying different sintering processes to densely packed materials with and without crystal growth. By changing the content of volatile lithium, we optimized the conditions for forming a stable cubic phase and explored variables such as temperature, pressure, and the amount of lithium added to optimize the conditions for achieving high ionic conductivity.

2. Materials and Methods

2.1. Preparation of Pure LLZO Powder and Pellets with Bed Powder

LLZO was synthesized via a solid-state reaction. $\text{LiOH}\cdot\text{H}_2\text{O}$ (99.0%, Sigma-Aldrich, St. Louis, MI, USA), La_2O_3 (99.9%, Sigma-Aldrich), and ZrO_2 (99.9%, Yakuri Pure Chemicals, 11-1 Kogashou Village, Uji City, Kyoto, Japan) were used as reagents, and they were dried in a vacuum oven at 110 °C for 2 h before calcination. To compensate for the loss of volatile lithium during synthesis, 10 mol% excess lithium was added to the reagent. Isopropyl alcohol was used as a solvent, and the container was filled with 50 zirconia balls of 10 mm size and ball milled for 4 h at a speed of 280 rpm. After ball milling, the reagents were air-dried in a hood and further dried in a vacuum oven at 80 °C. The dried powder was ground in a mortar, placed in an alumina crucible, and calcined in an electric furnace at a temperature increase rate of 850 °C and 2 °C per minute for 16 h. To sinter the calcined powder, an excess of 100 mol% lithium was added to compensate for lithium loss during high-temperature sintering. A 100 mol% excess lithium was prepared using $\text{LiOH}\cdot\text{H}_2\text{O}$ and dried using the same procedure as described above. Afterwards, secondary ball milling and drying were performed using the same process parameters as above. After crushing the dried powder with a mortar and sieving it into fine powder, 0.5 g of the powder was taken, and pellets were manufactured at a pressure of 30 MPa using a hydraulic press while maintaining the pressure for 3 min using a mold with a diameter of 16 mm. The pellets in rubber bags were then vacuum sealed and subjected to secondary compression at 200 MPa using a cold isostatic press (CIP).

2.2. Sintering

Alumina powder was spread on an alumina plate to create a tunnel with a horizontal distance of 0.5 cm. Unlike most published literature, in this work, instead of covering the pellet, the mother powder was placed approximately 15 mm away from the pellet (see Figure 1). That is why mother powder is also called bed powder. To compensate for lithium loss during high-temperature sintering, bed powder was spread in a circular shape in the range of 0 to 0.6 g. Afterwards, the pellet was placed on top of the alumina powder, the crucible was covered with a lid to maintain a uniform lithium atmosphere, and then it was sintered in an electric furnace. The sintering temperature was increased to 790–850 °C at a rate of 2 °C per minute and maintained for 7–8 h.

2.3. Characterization

For phase analysis of sintered powder and sintered pellets, X-ray diffraction (XRD, Smartlab SE, Korea I.T.S. Co., Ltd., 174-10 Jagok-ro, Gangnam-gu, Seoul, Republic of Korea) was used in the θ -2 θ range from 10° to 60°. The ionic conductivity of the fabricated samples was measured using electrochemical impedance spectroscopy (EIS, Iviumstat, HS technologies, 643-12, Gosan-ro, Gunpo-si, Gyeonggi-do, Republic of Korea). To measure ionic conductivity, the sample surface was polished smooth with 800 mesh, 1200 mesh, and 2000 mesh SiC paper. To avoid erroneously observing impurities other than the actual sample surface, the sample surface was etched using 3 M HCl. Gold electrodes (Au) were sputtered on both sides of the sample using a sputter deposition process. Ionic conductivity was calculated from EIS measurements at room temperature. To analyze the surface morphology and elemental composition of the sample, scanning electron microscopy (SEM), energy dispersive X-ray spectroscopy (EDS), and inductively coupled plasma atomic emission spectroscopy (ICP-AES) were used.



Figure 1. Image of sample in the setup after sintering without contact with the bed powder.

3. Results

3.1. Optimization of the Synthesis

Figure 2 shows the XRD pattern of a sample calcined at 850 °C for 16 h, in which only the tetragonal phase is observed. In order to form a cubic phase, lithium must be added to replenish the lithium lost during sintering and to optimize sintering conditions. By keeping the sintering conditions constant throughout the process, we were able to optimize the sintering conditions to obtain a pure cubic phase. To set the synthesis conditions of the cubic phase, three variables were considered: sintering temperature, sintering time, and lithium content.

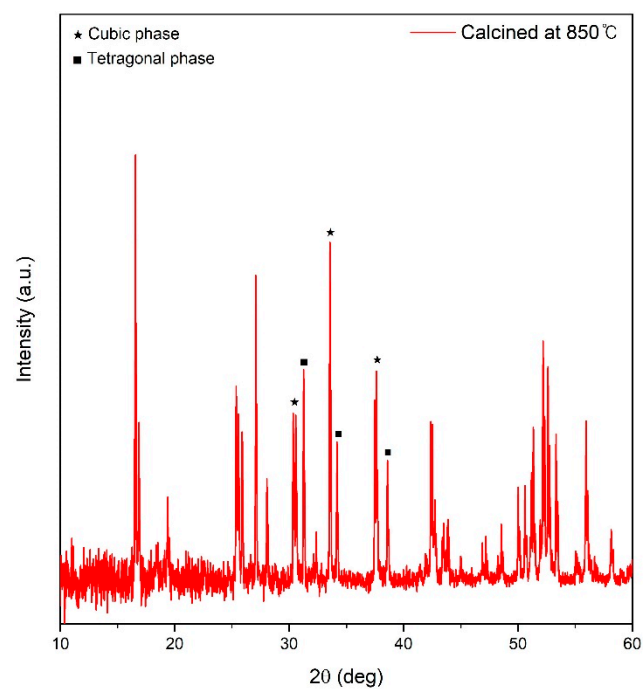


Figure 2. XRD pattern after calcining at 850 °C, 16 h.

3.1.1. Sintering Temperature

Figure 3 shows the XRD patterns of samples sintered at various temperatures from 790 °C to 850 °C using excess LiOH powder for 8 h. In the XRD patterns of samples sintered below 800 °C, only the tetragonal phase of LLZO is observed. In the XRD pattern at 800 °C, significant amounts of $\text{La}_2\text{Zr}_2\text{O}_7$ (LZO) begin to be observed, and weak intensity peaks of the cubic phase begin to appear. It is clear that the cubic phase can form at 800 °C. However, lithium deficiency results in the formation of significant amounts of LZO. At temperatures higher than 800 °C, specifically 850 °C, only the peak of LZO is observed in the XRD pattern, and no additional peaks are observed. Therefore, the optimal temperature for cubic phase formation is 800 °C. At low temperatures, the tetragonal phase is the main phase, and at high temperatures, LZO is formed due to excessive lithium loss.

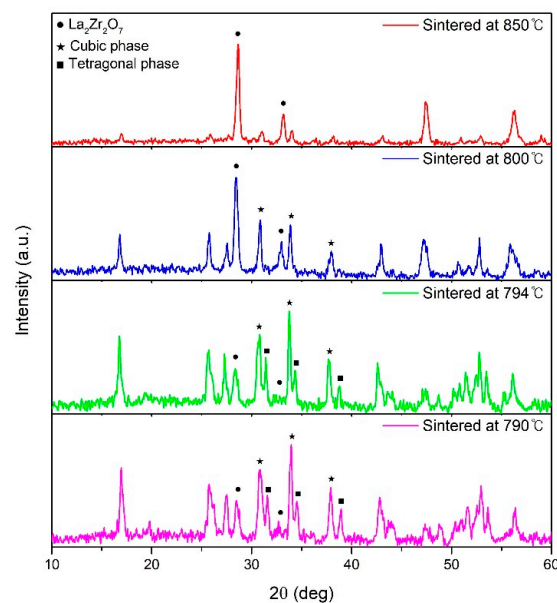


Figure 3. XRD patterns after different sintering temperatures, 8 h of sintering without bed powder.

3.1.2. Duration of Sintering

Minimizes lithium loss at the optimal temperature of 800 °C. The sintering period is an important factor affecting the formation of the cubic phase. The longer the duration, the easier the atoms diffuse to each lattice site, but the greater the lithium loss. Figure 4 shows the XRD patterns for varying sintering periods from 7 to 8 h at 800 °C. The XRD pattern showed that both the cubic phase and LZO were formed for 8 h, and the tetragonal phase and LZO were observed simultaneously for less than 8 h. Given these experimental results, it is expected that exceeding 8 h will cause excessive lithium loss and lead to additional LZO formation. Therefore, the optimal sintering time at 800 °C was determined to be 8 h.

3.1.3. Amount of Bed Powder

Compensating for lithium is essential to achieve a purer cubic-phase LLZO and reduce the LZO peak in the XRD pattern. A common way to compensate for lithium in conventional high-temperature sintering processes for cubic-phase LLZO formation is to use mother powder covering, as was used for early LLZO synthesis [33]. However, recent studies have explored sintering without the use of covering powder [25,34–38]. To compensate for lithium under the optimized conditions shown in Figure 4, non-covering powder sintering using bed powder was used, as illustrated in Figures 1 and 5. Figure 5 is a digital image after placing mother powder directly under the contacted pellet and sintering. Figure 1 shows a digital image after sintering by placing the pellets on top of the alumina powder and placing the bed powder on the outside of the alumina so that it does

not contact the pellets. Sintering conditions were consistently applied to the optimized conditions (800 °C, 8 h) shown in Figure 4.

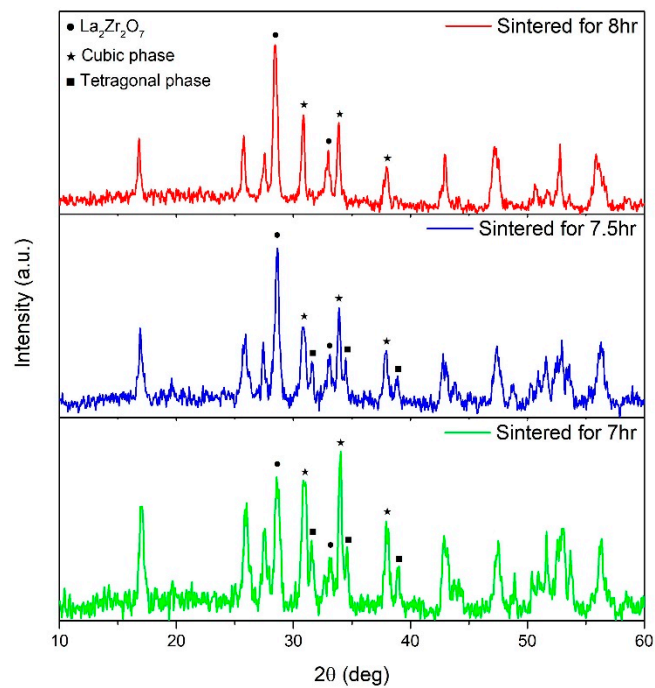


Figure 4. XRD patterns after different sintering times at 800 °C without bed powder.



Figure 5. Image of sample in the setup after sintering while in contact with the mother powder.

Figure 6 displays the XRD patterns of samples sintered under the conditions in Figures 1 and 5, comparing those with and without contact between the bed powder and the pellets. The absence of LZO peaks in both results suggests successful compensation for lithium, highlighting the effectiveness of the sintering process in replenishing and maintaining lithium within the LLZO sample. In the XRD pattern of the sample sintered in direct contact with bed powder, both cubic and tetragonal phases were observed, but

the XRD pattern of the sample sintered without contact with bed powder showed pure cubic-phase LLZO. This means that adopting the setup method described in Figure 1, which is characterized by the absence of direct contact between bed powder and pellets, increases the possibility of producing purer cubic-phase LLZO.

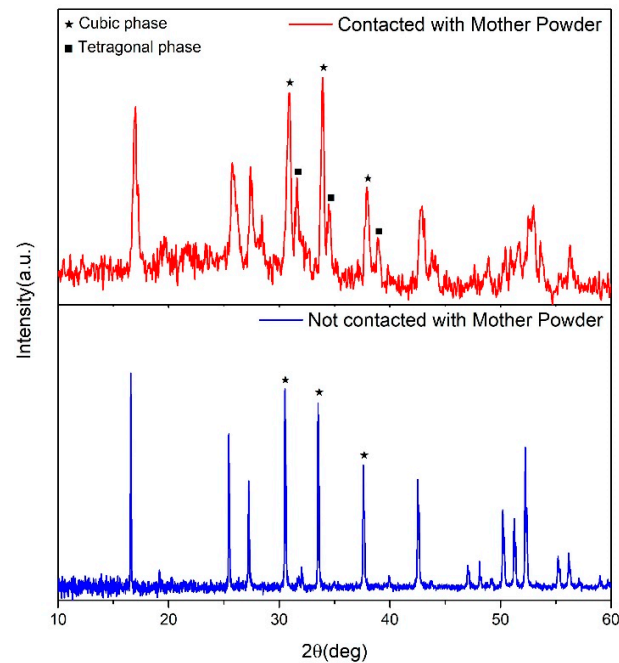


Figure 6. XRD patterns after sintering at 800 °C, 8 h using distinct experimental setups.

To investigate the effect of bed powder on the sintering process and further optimize the production of pure cubic-phase LLZO, experiments were performed by varying the amount of bed powder from 0 g to 0.6 g. Bed powder was used as described in Figure 1. Bed powder serves to supplement Li in the sample by forming an Li atmosphere inside the alumina crucible lid during sintering. Figure 7 shows the XRD patterns for each bed powder amount. The XRD pattern indicates the co-formation of cubic phases and LZO at bed powder amounts below 0 g, the formation of purer cubic phases at 0.3 g and 0.4 g, and the formation of tetragonal phases above 0.5 g. Comparing the XRD patterns of the cubic phase formed between 0.3 g and 0.4 g, the pattern at 0.4 g is closer to that of the pure cubic phase. Therefore, under 8 h sintering conditions at 800 °C, the optimal amount of bed powder is determined to be 0.4 g.

3.1.4. Structural Uniformity

To confirm the structural uniformity of the cubic LLZO synthesized under optimal conditions (sintering temperature 800 °C, sintering time 8 h, bed powder 0.4 g), the top and bottom surfaces of the specimen were separated and the XRD pattern was analyzed. Figure 8 shows the XRD pattern for the top and bottom surfaces of the specimen. Comparing the XRD patterns of the strong intensity of the cubic phase formed on the top and bottom surfaces, it is observed that only a weak LZO phase is formed on the bottom surface. This means that there is not enough lithium to form a cubic phase in the lower part compared to the upper part of the sintered specimen under optimized conditions. The presence of alumina powder is expected to prevent the bottom surface from creating a lithium atmosphere, preventing proper lithium replenishment.

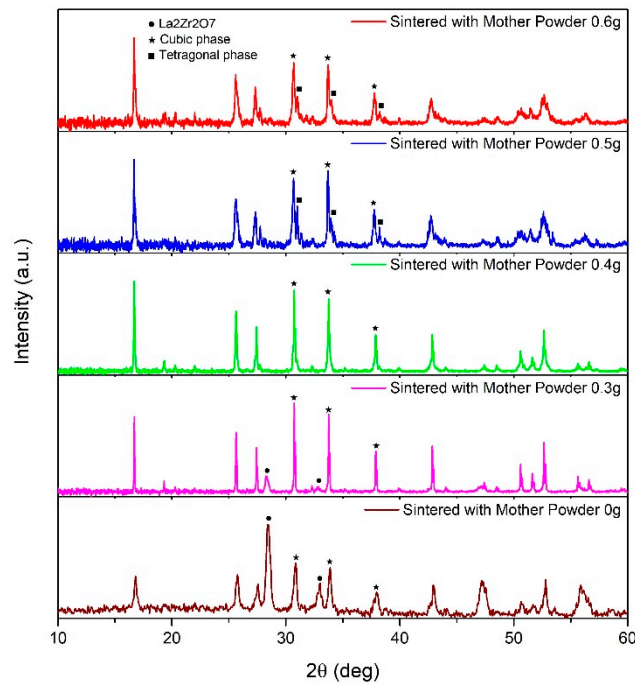


Figure 7. XRD patterns after sintering at 800 °C, 8 h using different amounts of bed powder.

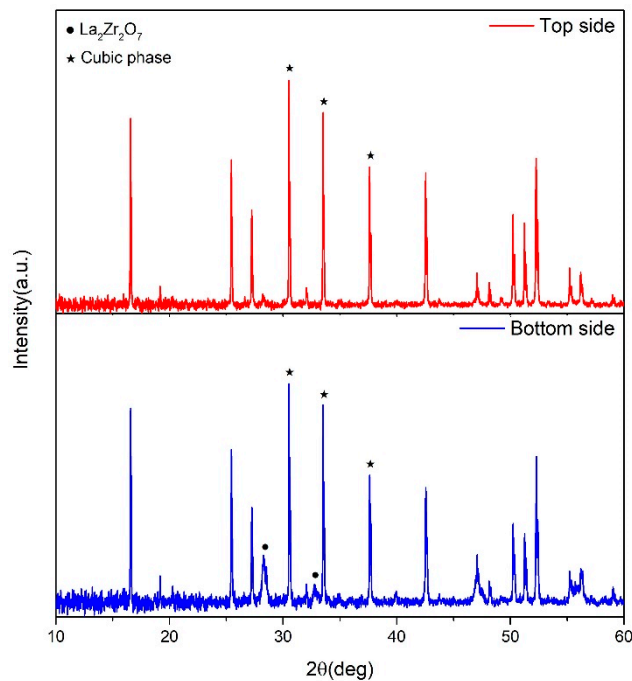


Figure 8. XRD pattern on both sides after sintering at 800 °C for 8 h using 0.4 g of bed powder.

Lack of lithium content or loss of lithium is known to be a variable that affects the ionic conductivity of garnet electrolyte [39,40]. For this reason, in order to obtain high ionic conductivity, it is important to minimize the lack of lithium content or lithium atmosphere, which causes LZO to form on the bottom surface of the specimen during the sintering step. To create a lithium atmosphere on the bottom surface and facilitate lithium replenishment, an additional tunnel was introduced between the specimen and the alumina powder to expose the bottom surface of the specimen to the lithium atmosphere. Figure 9 shows the geometry of the specimen on alumina powder before sintering, with additional tunnels created to form a lithium atmosphere on the bottom surface.

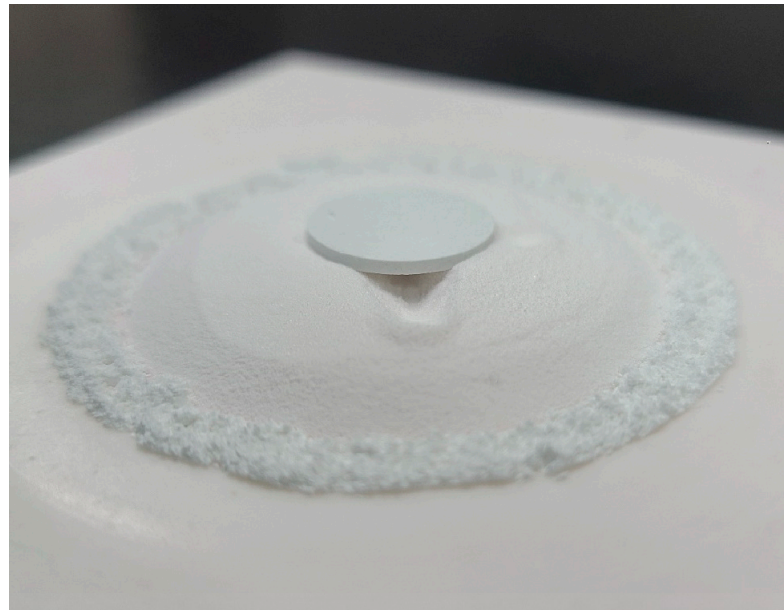


Figure 9. Pre-sintering samples that created a 0.5 cm wide tunnel.

A 0.5 cm horizontal tunnel was created between the alumina powder and the specimen, and sintering was performed under the same conditions as above. Figure 10 shows the XRD pattern of a specimen sintered at 800 °C for 8 h using 0.4 g of bed powder, showing the top and bottom sides separately. In the sample without a tunnel, a weak LZO was formed on the bottom surface and a pure cubic phase was formed on the top surface, while the sample with a 0.5 cm tunnel on both sides showed the formation of a pure cubic phase on both sides. This suggests that the formation of a lithium atmosphere on the bottom surface was promoted by forming a 0.5 cm tunnel between the alumina powder and the specimen during sintering, enabling sufficient lithium replenishment and improving structural uniformity.

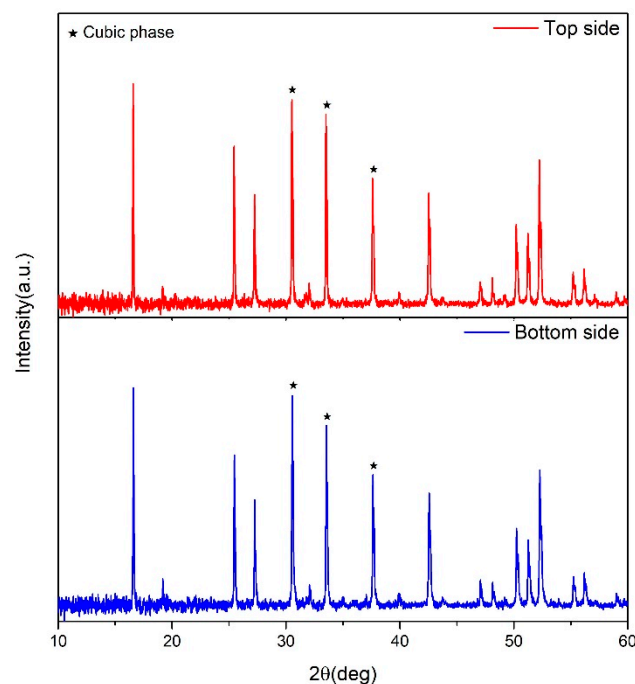


Figure 10. XRD pattern on both sides after sintering at 800 °C for 8 h using 0.4 g of bed powder with 0.5 cm wide tunnel between the specimen and alumina powder.

Table 1 summarizes the variables set during the optimization process and the steps formed from those variables. The optimization process systematically considered three key variables: Sintering temperature, sintering time, and bed powder amount. First, the most suitable temperature for cubic-phase formation is 800 °C. At 800 °C, both the cubic phase and LZO were formed, but below 800 °C, the tetragonal phase and LZO were formed, and above 800 °C, LZO was formed due to excessive lithium loss. Second, the optimal sintering time is 8 h. At 8 h, the cubic phase and LZO were formed together, but below 8 h, the tetragonal phase and LZO were formed together due to little lithium volatilization. Third, non-covering-powder sintering was used by adding bed powder to compensate for lithium loss, and the optimal amount is 0.4 g. At 0.4 g, only the cubic phase was formed, but at less than 0.4 g, both the cubic phase and LZO were formed, and at more than 0.4 g, only the tetragonal phase was formed. This indicates that adding 0.4 g of bed powder can sufficiently replenish lithium to prevent unwanted LZO formation. Finally, the structural uniformity of the samples was checked. Since a small amount of LZO was formed on the bottom surface of the sample prepared under the above conditions, a 0.5 cm wide tunnel was created between the sample and the alumina powder during sintering to form the same phase on both sides. This modification creates a lithium atmosphere on the bottom side of the sample, creating equally pure cubic phases on both sides and improving structural uniformity. Ultimately, the optimized parameters for cubic-phase formation were sintering at 800 °C for 8 h using 0.4 g of bed powder and a 0.5 cm wide tunnel between the sample and the alumina powder. The items highlighted in bold indicate the variables that are optimized in each step, while the remaining items indicate variables that form unwanted steps.

Table 1. Formation of LLZO phases under various sintering conditions.

Process	Constant Condition	Variable	Phase
Sintering temperature	8 h, without bed powder	790 °C	Tetragonal + LZO
		794 °C	Tetragonal + LZO
		800 °C	Cubic + LZO
		850 °C	LZO
Duration of sintering	800 °C, without bed powder	7 h	Tetragonal + LZO
		7.5 h	Tetragonal + LZO
		8 h	Cubic + LZO
Amount of bed powder	800 °C, 8 h with bed powder	0 g	Cubic + LZO
		0.3 g	Cubic + LZO
		0.4 g	Cubic
		0.5 g	Tetragonal
		0.6 g	Tetragonal
Structural uniformity	800 °C, 8 h, 0.4 g of bed powder	No tunnel	Top: Cubic Bottom: Cubic + LZO
		Tunnel width of 0.5 cm	Top: Cubic Bottom: Cubic

3.2. SEM, EDS, and ICP-AES Analysis

3.2.1. SEM Analysis

Figure 11 shows SEM images of samples sintered under optimized conditions. In Figure 11a,b, one can observe irregular blocks with a typical particle size distribution of 2–3 µm and an overall agglomeration of small particles. Additionally, some pores can be seen scattered between the particles. As can be seen from the microstructure, it is expected that the cubic phase will be well formed through sufficient pores and inter-particle contact.

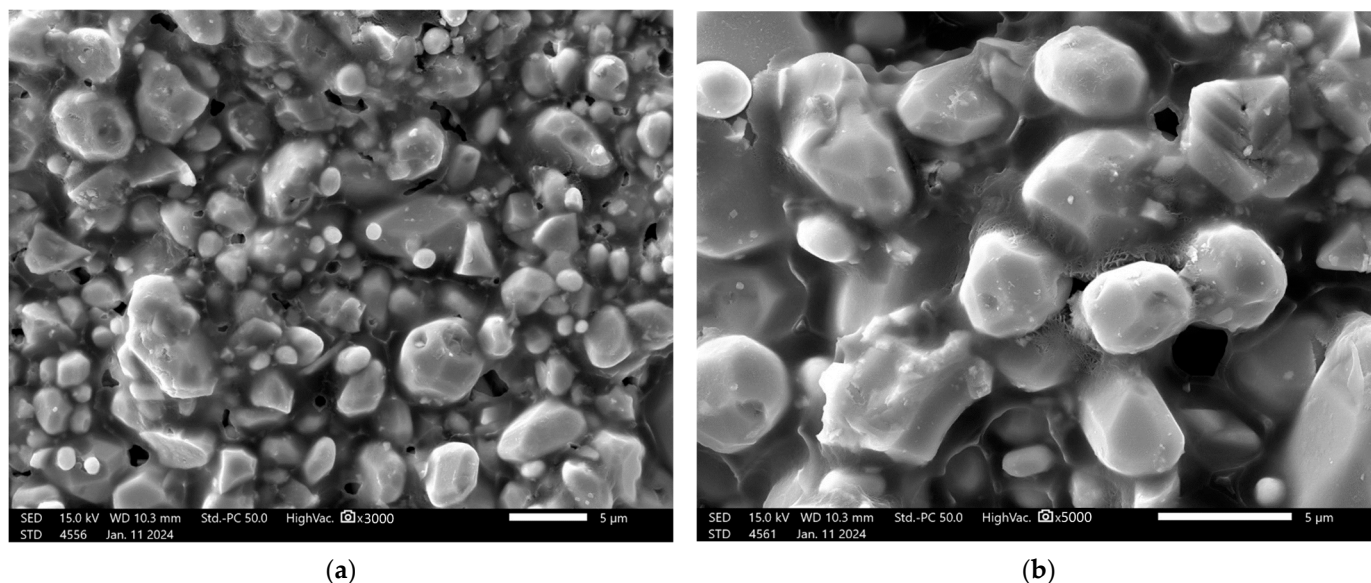


Figure 11. SEM images of LLZO sintered at 800 °C for 8 h using 0.4 g of bed powder. (a) 3000× magnification, (b) 5000× magnification.

3.2.2. EDS Analysis

Figure 12 shows the EDS mapping results of samples sintered under optimized conditions. The SEM micrograph at 1000× magnification shown in Figure 12a–d shows the distribution of La (purple), Zr (green), and O (red) in the EDS elemental map. EDS results show a uniform distribution of La, Zr, and O throughout the image. Table 2 provides the phase composition of samples sintered under optimized conditions. Due to measurement limitations, the lithium content is unknown, but since the La:Zr ratio is 3:2, it can be assumed that LLZO maintains a 7:3:2:12 ratio.

Table 2. Phase compositions of LLZO sintered at 800 °C for 8 h using 0.4 g of bed powder.

Magnification	Element	Mass (%)	Atom (%)
1000×	La	51.41 ± 0.50	16.48 ± 0.16
	Zr	22.52 ± 0.18	10.99 ± 0.09
	O	26.06 ± 0.10	72.53 ± 0.27

3.2.3. ICP-AES Analysis

We analyzed the elements of LLZO in two cubic samples showing a clean cubic phase by ICP-AES. As shown in Table 3, the elemental composition is close to the expected stoichiometric ratio of $\text{Li}_7\text{La}_3\text{Zr}_2\text{O}_{12}$. The chemical formula of the synthesized LLZO is calculated as $\text{Li}_{8.2}\text{La}_3\text{Zr}_2\text{O}_{12}$ and $\text{Li}_{8.3}\text{La}_3\text{Zr}_2\text{O}_{12}$, which indicates a small content of excess lithium, giving a pure cubic phase. This is consistent with the EDS result. If the lithium content is higher than this value, the tetragonal phase is indicated. Conversely, if the lithium content is lower than this value, the LZO phase is formed.

Table 3. Weight% of the elements in LLZO was determined through ICP-AES analysis and compared with the theoretical stoichiometry.

Element	Theoretical wt%	Experimental wt% Sample #1	Experimental wt% Sample #2
Li	5.79	5.68	5.77
La	49.63	42.3	42.2
Zr	21.71	18.7	18.7

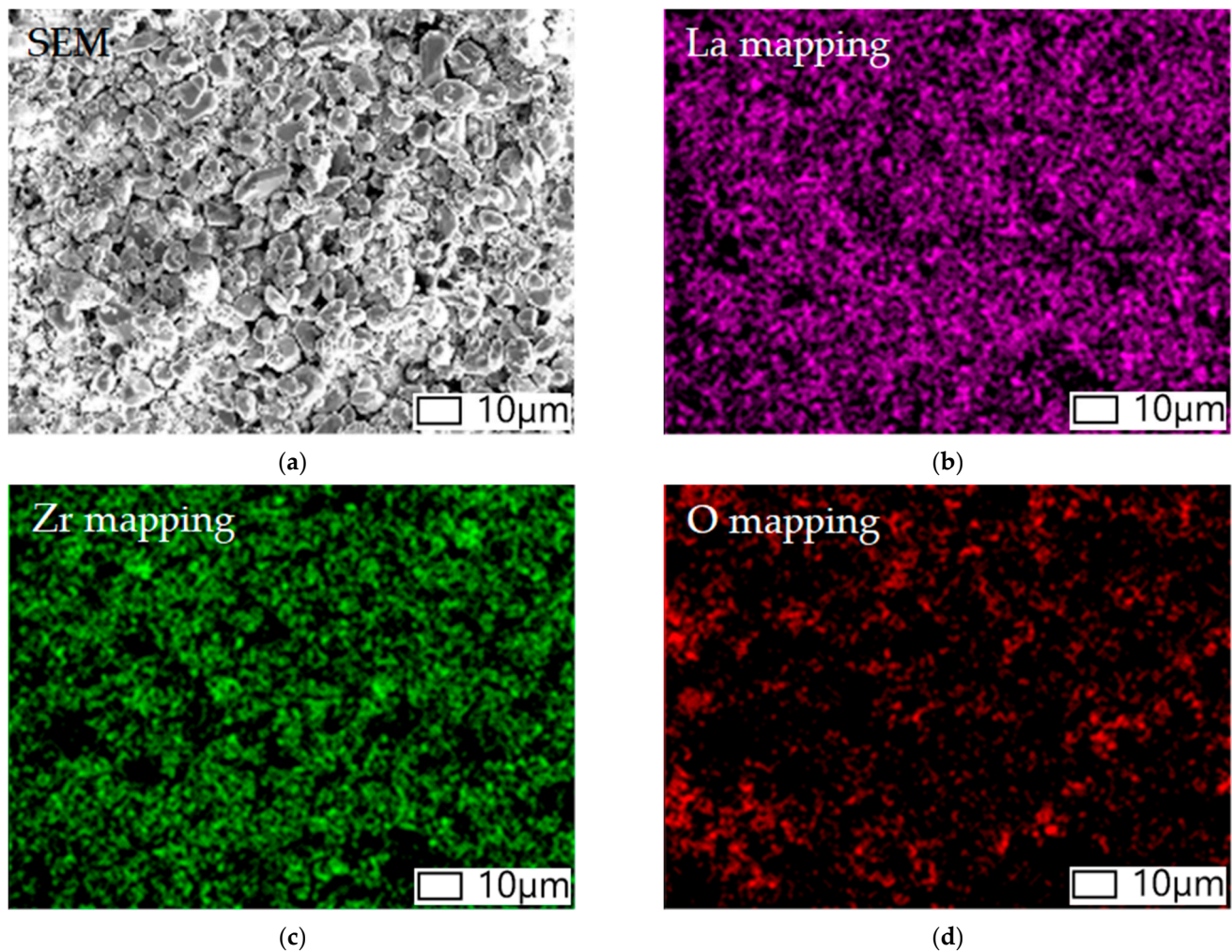


Figure 12. EDS images at different magnifications: (a) SEM image at 1000 \times , (b) La mapping at 1000 \times , (c) Zr mapping at 1000 \times , (d) O mapping at 1000 \times .

3.3. Ionic Conductivity

The impedance plot at room temperature is shown in Figure 13, with the simulation results shown as solid lines. In the high-frequency region, a single semicircle exists, and there is no difference between bulk resistance and grain boundary resistance. In the low-frequency tail, a rising line appears due to the blocking electrode (Au), which blocks lithium ions but not electrons. The experimental data were fitted with an equivalent circuit composed of $(R_g CPE_g)(R_{gb} CPE_{gb})(R_{el})$ where R_g is resistance of grain, CPE_g is constant phase element of grain, R_{gb} is resistance of grain boundary, CPE_{gb} is constant phase element of grain boundary, and R_{el} is resistance of electrode. The subscripts g, gb, and el refer to grains, grain boundaries, and electrodes. The total resistance ($R_{total} = R_g + R_{gb}$), calculated as the value corresponding to the x-intercept of the plot, yields an ionic conductivity value of approximately $2.53 \times 10^{-5} \text{ S cm}^{-1}$.

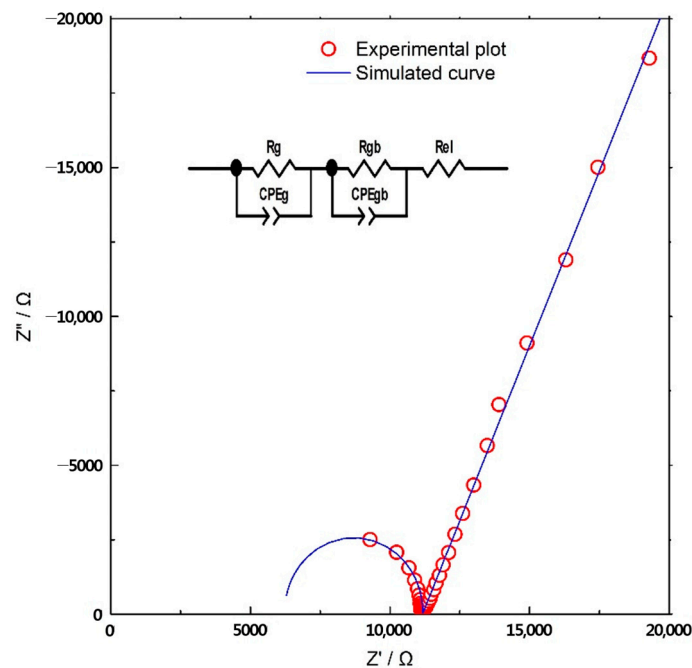


Figure 13. Impedance plot of LLZO synthesized at optimized conditions. EIS result measured at room temperature with a 0.5 V DC voltage applied to the Au/LLZO/Au symmetric cell.

4. Conclusions

In this study, we established optimal conditions for manufacturing cubic-phase LLZO, an all-solid-state battery electrolyte. The formation conditions of the cubic phase were investigated by changing the synthesis temperature and duration. In particular, the focus was on establishing the formation conditions of pure cubic-phase LLZO by varying the amount of bed powder to compensate for lithium loss due to high-temperature sintering. This study confirmed that sintering at 800 °C for 8 h is the optimal temperature and duration for manufacturing cubic-phase LLZO. By optimizing the amount of bed powder, impurities such as LZO and tetragonal phase were prevented, and pure cubic-phase LLZO was obtained. This study showed that pure cubic-phase LLZO can be reliably prepared at a lower temperature (800 °C) compared to previous reports that focused on producing pure cubic-phase LLZO at temperatures exceeding 1100 °C. Additionally, a sintering process was developed to create a lithium atmosphere on the bottom surface and facilitate lithium replenishment, and an additional tunnel was introduced between the specimen and the alumina powder to ensure that the bottom surface of the specimen was exposed to the lithium atmosphere. It was confirmed that a cubic phase was formed on both sides of the sample. By manufacturing a uniform electrolyte, it was possible to open the way to manufacturing an all-solid-state battery. The findings provide valuable insights into the important synthetic parameters involved in producing undoped cubic-phase LLZO. This will provide a standard for synthesizing LLZO with higher ionic conductivity through doping or modification of other parameters. Based on this, it shows wide applicability in manufacturing solid electrolytes for batteries.

Author Contributions: Supervision, project administration, funding acquisition, writing—review and editing, D.-M.K.; conceptualization, methodology, investigation, validation, software, writing—original draft preparation, T.P.; visualization, methodology, data interpretation, software, writing—original draft preparation, S.L. All authors have read and agreed to the published version of the manuscript.

Funding: This research was funded by [Korea Government Ministry of Science and ICT(MSIT)] grant number [RS-2022-00156291].

Data Availability Statement: The original contributions presented in the study are included in the article, further inquiries can be directed to the corresponding authors.

Conflicts of Interest: The authors declare no conflicts of interest.

References

1. Tarascon, J.-M.; Armand, M. Issues and challenges facing rechargeable lithium batteries. *Nature* **2001**, *414*, 359–367. [[CrossRef](#)]
2. Zubi, G.; Dufó-López, R. The lithium-ion battery: State of the art and future perspectives. *Renew. Sustain. Energy Rev.* **2018**, *89*, 292–308. [[CrossRef](#)]
3. Wen, J.; Yu, Y. A review on lithium-ion batteries safety issues: Existing problems and possible solutions. *Mater. Express* **2012**, *2*, 197–212. [[CrossRef](#)]
4. Wang, Q.; Jiang, L. Progress of enhancing the safety of lithium ion battery from the electrolyte aspect. *Nano Energy* **2019**, *55*, 93–114. [[CrossRef](#)]
5. Roth, E.P.; Orendorff, C.J. How electrolytes influence battery safety. *Electrochem. Soc. Interface* **2012**, *21*, 45. [[CrossRef](#)]
6. Jung, Y.C.; Kim, S.K. Ceramic separators based on Li⁺-conducting inorganic electrolyte for high-performance lithium-ion batteries with enhanced safety. *J. Power Sources* **2015**, *293*, 675–683. [[CrossRef](#)]
7. Hayashi, A.; Tatsumisago, M. Recent development of bulk-type solid-state rechargeable lithium batteries with sulfide glass-ceramic electrolytes. *Electron. Mater. Lett.* **2012**, *8*, 199–207. [[CrossRef](#)]
8. Hatzell, K.B.; Chen, X.C. Challenges in lithium metal anodes for solid-state batteries. *ACS Energy Lett.* **2020**, *5*, 922–934. [[CrossRef](#)]
9. Agrawal, R.C.; Pandey, G.P. Solid polymer electrolytes: Materials designing and all-solid-state battery applications: An overview. *J. Phys. D Appl. Phys.* **2008**, *41*, 223001. [[CrossRef](#)]
10. Banerjee, A.; Wang, X. Interfaces and interphases in all-solid-state batteries with inorganic solid electrolytes. *Chem. Rev.* **2020**, *120*, 6878–6933. [[CrossRef](#)]
11. Lim, H.D.; Park, J.H. A review of challenges and issues concerning interfaces for all-solid-state batteries. *Energy Storage Mater.* **2020**, *25*, 224–250. [[CrossRef](#)]
12. Diederichsen, K.M.; McShane, E.J. Promising routes to a high Li⁺ transference number electrolyte for lithium ion batteries. *ACS Energy Lett.* **2017**, *2*, 2563–2575. [[CrossRef](#)]
13. Zhao, N.; Khokhar, W. Solid garnet batteries. *Joule* **2019**, *3*, 1190–1199. [[CrossRef](#)]
14. He, L.; Oh, J.A.S. Synthesis and interface modification of oxide solid-state electrolyte-based all-solid-state lithium-ion batteries: Advances and perspectives. *Funct. Mater. Lett.* **2021**, *14*, 2130002. [[CrossRef](#)]
15. Ji, W.; Luo, B. A review of challenges and issues concerning interfaces for garnet-type all-solid-state batteries. *J. Alloys Compd.* **2024**, *2024*, 173530. [[CrossRef](#)]
16. Awaka, J.; Takashima, A. Crystal structure of fast lithium-ion-conducting cubic Li₇La₃Zr₂O₁₂. *Chem. Lett.* **2011**, *40*, 60–62. [[CrossRef](#)]
17. Awaka, J.; Kijima, N. Synthesis and structure analysis of tetragonal Li₇La₃Zr₂O₁₂ with the garnet-related type structure. *J. Solid State Chem.* **2009**, *182*, 2046–2052. [[CrossRef](#)]
18. Chen, F.; Li, J. Origin of the phase transition in lithium garnets. *J. Phys. Chem. C* **2018**, *122*, 1963–1972. [[CrossRef](#)]
19. Chen, C.; Wang, K. Processing and Properties of Garnet-Type Li₇La₃Zr₂O₁₂ Ceramic Electrolytes. *Small* **2023**, *19*, 2205550. [[CrossRef](#)]
20. Chen, C.; Sun, Y. Microstructural and electrochemical properties of Al- and Ga-doped Li₇La₃Zr₂O₁₂ garnet solid electrolytes. *ACS Appl. Energy Mater.* **2020**, *3*, 4708–4719. [[CrossRef](#)]
21. Kotobuki, M.; Yan, B. Study on stabilization of cubic Li₇La₃Zr₂O₁₂ by Ge substitution in various atmospheres. *Funct. Mater. Lett.* **2016**, *9*, 1642005. [[CrossRef](#)]
22. Lei, C.; Shetty, D.K. Fabrication of high-density and translucent Al-containing garnet, Li_{7-x}La₃Zr_{2-x}Ta_xO₁₂ (LLZTO) solid-state electrolyte by pressure filtration and sintering. *Solid State Ion.* **2021**, *364*, 115640. [[CrossRef](#)]
23. Hamao, N.; Hamamoto, K. Fabrication of single-grain-layered garnet-type electrolyte sheets by a precursor method. *J. Asian Ceram. Soc.* **2022**, *10*, 1–8. [[CrossRef](#)]
24. Rettenwander, D.; Redhammer, G. Structural and electrochemical consequences of Al and Ga cosubstitution in Li₇La₃Zr₂O₁₂ solid electrolytes. *Chem. Mater.* **2016**, *28*, 2384–2392. [[CrossRef](#)]
25. Huang, X.; Lu, Y. None-mother-powder method to prepare dense Li-garnet solid electrolytes with high critical current density. *ACS Appl. Energy Mater.* **2018**, *1*, 5355–5365. [[CrossRef](#)]
26. Kotobuki, M.; Hanc, E. Stabilization of cubic Li₇La₃Zr₂O₁₂ by Al substitution in various atmospheres. *Solid State Ion.* **2020**, *350*, 115323. [[CrossRef](#)]
27. Matsui, M.; Takahashi, K. Phase stability of a garnet-type lithium ion conductor Li₇La₃Zr₂O₁₂. *Dalton Trans.* **2014**, *43*, 1019–1024. [[CrossRef](#)]
28. Thompson, T.; Wolfenstine, J. Tetragonal vs. cubic phase stability in Al-free Ta doped Li₇La₃Zr₂O₁₂ (LLZO). *J. Mater. Chem. A* **2014**, *2*, 13431–13436. [[CrossRef](#)]
29. Kokal, I.; Somer, M. Sol-gel synthesis and lithium ion conductivity of Li₇La₃Zr₂O₁₂ with garnet-related type structure. *Solid State Ion.* **2011**, *185*, 42–46. [[CrossRef](#)]

30. Xie, H.; Li, Y. Low-temperature synthesis of $\text{Li}_7\text{La}_3\text{Zr}_2\text{O}_{12}$ with cubic garnet-type structure. *Mater. Res. Bull.* **2012**, *47*, 1229–1232. [[CrossRef](#)]
31. Heo, T.W.; Grieder, A. Microstructural impacts on ionic conductivity of oxide solid electrolytes from a combined atomistic-mesoscale approach. *NPJ Comput. Mater.* **2021**, *7*, 214. [[CrossRef](#)]
32. Yu, S.; Siegel, D.J. Grain boundary contributions to Li-ion transport in the solid electrolyte $\text{Li}_7\text{La}_3\text{Zr}_2\text{O}_{12}$ (LLZO). *Chem. Mater.* **2017**, *29*, 9639–9647. [[CrossRef](#)]
33. Murugan, R.; Thangadurai, V. Fast lithium ion conduction in garnet-type $\text{Li}_7\text{La}_3\text{Zr}_2\text{O}_{12}$. *Angew. Chem. Int. Ed.* **2007**, *46*, 7778–7781. [[CrossRef](#)]
34. Ji, Y.; Zhou, C. Submicron-sized Nb-doped lithium garnet for high ionic conductivity solid electrolyte and performance of quasi-solid-state lithium battery. *Materials* **2020**, *13*, 560. [[CrossRef](#)]
35. Matsuda, Y.; Sakaida, A. Sintering behavior and electrochemical properties of garnet-like lithium conductor $\text{Li}_{6.25}\text{M}_{0.25}\text{La}_3\text{Zr}_2\text{O}_{12}$ (M: Al^{3+} and Ga^{3+}). *Solid State Ion.* **2017**, *311*, 69–74. [[CrossRef](#)]
36. Yang, L.; Dai, Q. Rapid sintering method for highly conductive $\text{Li}_7\text{La}_3\text{Zr}_2\text{O}_{12}$ ceramic electrolyte. *Ceram. Int.* **2020**, *46*, 10917–10924. [[CrossRef](#)]
37. Yang, L.; Tao, X. Efficient mutual-compensating Li-loss strategy toward highly conductive garnet ceramics for Li-metal solid-state batteries. *ACS Appl. Mater. Interfaces* **2021**, *13*, 56054–56063. [[CrossRef](#)]
38. Hosokawa, H.; Takeda, A. Tolerance for Li dendrite penetration in Ta-doped $\text{Li}_7\text{La}_3\text{Zr}_2\text{O}_{12}$ solid electrolytes sintered with $\text{Li}_{2.3}\text{C}_{0.7}\text{B}_{0.3}\text{O}_3$ additive. *Mater. Lett.* **2020**, *279*, 128481. [[CrossRef](#)]
39. Huang, X.; Lu, Y. Manipulating Li_2O atmosphere for sintering dense $\text{Li}_7\text{La}_3\text{Zr}_2\text{O}_{12}$ solid electrolyte. *Energy Storage Mater.* **2019**, *22*, 207–217. [[CrossRef](#)]
40. Thompson, T.; Sharafi, A. A tale of two sites: On defining the carrier concentration in garnet-based ionic conductors for advanced Li batteries. *Adv. Energy Mater.* **2015**, *5*, 1500096. [[CrossRef](#)]

Disclaimer/Publisher’s Note: The statements, opinions and data contained in all publications are solely those of the individual author(s) and contributor(s) and not of MDPI and/or the editor(s). MDPI and/or the editor(s) disclaim responsibility for any injury to people or property resulting from any ideas, methods, instructions or products referred to in the content.